2021 S.T. Yau High School Science Award (Asia)

Research Report

Registration Number: Phy-056

Name of team member: Tu Yaowei
School: Raffles Institution
City, Country: Singapore

Name of team member: Yang Liu
School: Raffles Institution
City, Country: Singapore

Name of supervising teacher: Ms Sze Guan Kheng
Job Title: Lead teacher of Physics department
School/Institution: Raffles Institution City, Country: Singapore

Title of Research Report

Astrojax Pendulum: Theoretical and Experimental Studies

Date

31 August 2021

1

Astrojax Pendulum: Theoretical and Experimental Studies

Tu Yaowei and Yang Liu

August 30, 2021

Abstract

An Astrojax pendulum is a system which has two spheres fixed at either ends of string and an additional sphere able to move freely along the string. When the top of the string is driven at a specific angular frequency by a motor, these two balls will trace out different motion patterns (eg. circular and flower motions). This work aims to explore this phenomenon in two stages: firstly, a comprehensive Lagrangian formulation which models the three-dimensional motion paths of both the middle and the bottom ball; secondly, an experimental verification of our model to elucidate the dynamic trajectories under various motor angular frequencies, including hysterisis in rising and falling mechanism, circular orbits, and flower motion. The onset of these trajectories are realised experimentally by varying motor's angular frequency. The effect of varying parameters, such as length of string and mass of balls, is investigated as well. The findings presented in this work help us to gain a deeper understanding of how the system of Astrojax toy differs from the double pendulum system most commonly found in college physics textbooks. The Astrojax pendulum is hence an extremely insightful class demonstration for introductory college physics courses on mechanics, as its construction is easy and inexpensive.

Keywords: Lagrangian Mechanics, Astrojax Pendulum, Nonlinear Dynamics, Method of Discretisation.

Acknowledgement

Commitments on Academic Honesty and Integrity

We hereby declare that we

1. are fully committed to the principle of honesty, integrity and fair play throughout the competition.
2. actually perform the research work ourselves and thus truly understand the content of the work.
3. observe the common standard of academic integrity adopted by most journals and degree theses.
4. have declared all the assistance and contribution we have received from any personnel, agency, institution, etc. for the research work.
5. undertake to avoid getting in touch with assessment panel members in a way that may lead to direct or indirect conflict of interest.
6. undertake to avoid any interaction with assessment panel members that would undermine the neutrality of the panel member and fairness of the assessment process.
7. observe the safety regulations of the laboratory(ies) where we conduct the experiment(s), if applicable.
8. observe all rules and regulations of the competition.
9. agree that the decision of YHSA(Asia) is final in all matters related to the competition.

We understand and agree that failure to honour the above commitments may lead to disqualification from the competition and/or removal of reward, if applicable; that any unethical deeds, if found, will be disclosed to the school principal of team member(s) and relevant parties if deemed necessary; and that the decision of YHSA(Asia) is final and no appeal will be accepted.

(Signatures of full team below)
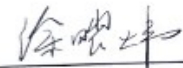
Name of team member: Tu Yaowei

Name of team member: Yang Liu

Name of team member:

Name of supervising teacher: Mr Sze Guan Kheng

Noted and endorsed by	
(signature)	REAVLEY MUNN YE (MRS) Deputy Principal, Academic Studies (Y5-6) Raffles Institution
Name of school principal:	

iii

2

Contents

1 Introduction

1.1 Background

Astrojax is a novel double pendulum system where the middle ball is allowed to move freely along the string with the bottom ball fixed at the end of the string (Fig. 1). The Astrojax toy has long been renowned as the "Future of The Yo-yo" [1] and emerged as part of NASA's Toys in Space education program [2]. Astrojax has also been a topic of interest for many research topics, such as chaos [3], nonlinear dynamics, and the N-body problem as applied to a sphere using complex computer modelling and advanced mathematics [4].

Figure 1: **Picture of the Astrojax toy.** Picture from *ThinkGreek*.

1.2 Literature Review

A comprehensive understanding of the basic double pendulum system has been established in many literature. For instance, Korsh and Dohl formulated the equations of motion for the planar double pendulum consists of two point masses attached to two massless rods of fixed lengths to demonstrate the non-linearity in the system [5]. The control of chaos and sensitivity analysis were also performed by A. Marcelo Tusset [6].

While reports on the standard double pendulum system have produced fruitful results, few have gone a step further to discuss the complex system of an Astrojax pendulum. In contrast to the traditional double pendulum with the middle ball being fixed on the string, the middle ball in the Astrojax pendulum is allowed to move freely along the string. In conjunction with the periodic motion of the point of suspension of string, four more degrees of freedom are introduced into this mechanical system. Some investigations have been carried out by past researchers. For instance, Karsai et al. have provided a purely qualitative study of the resultant frequencies of the middle and bottom balls [7]. Moreover, the Lagrangian mechanics was exploited by Toit in providing a in-depth study of reduction theory, variational integrators, and pattern evocation in the Astrojax pendulum [8]. However, these existing research are either overly qualitative and lack rigor in theoretical modelling, or too mathematically intensive and lack experimental verification. The periodic movement of the point of suspension was rarely investigated as well. Even though in [9], Dichter and Maschan have tried to circumvent these problems by offering a model to predict the motion of the two balls with the top of the string held stationary or undergoing random motion introduced by hand, a significant deviation between the theoretical and experimental results was observed, and detailed investigation into the systematic motion paths of the balls was absent. Therefore, this study serves to contribute to existing literature by modelling the motion of hand as a circular orbit and providing a comprehensive theoretical and experimental comparison to validate our quantitative model.

1.3 Section Overview

This work aims to explore the behaviour of the Astrojax pendulum both experimentally and theoretically in a more comprehensive and rigorous manner. In Section 2, we make use of Lagrangian mechanics with constraints imposed by conservation of total length of string to obtain the general equations of motion of the Astrojax pendulum. The method of discretisation is introduced to allow the equations obtained to be numerically solvable by any software with high computational efficiency. The constants involved in the calculation are experimentally measured with simple experiments as well. In Section 3, we verify our theoretical model with experiments on the circular and the flower orbits of the two balls. An analysis is also provided on the effect of parameters on the circular orbit, such as total length of string and mass of balls. In Section 4, some insightful future work is proposed to deepen the understanding of the Astrojax system in terms of the time-dependent evolution of its motion paths.

2 Quantitative Analysis

In this section, we will derive the governing equations of motion of the Astrojax pendulum via Lagrangian mechanics. These equations are then solved numerically by *MATHEMATICA* using the Euler's method with time step of $1/2000$ to obtain the coordinates of the two balls.

2.1 Coordinate and Variable Definition

Considering the Astrojax pendulum with total length of string l and mass of both balls m, we define the coordinates of the point of suspension as (a_x, a_y, a_z), and those of the middle ball and the bottom ball as (x_1, y_1, z_1) and (x_2, y_2, z_2) respectively as shown in Fig. 2(d). Therefore, we arrive at the general coordinates of the system as

$$q = (x_1, y_1, z_1, x_2, y_2, z_2)$$
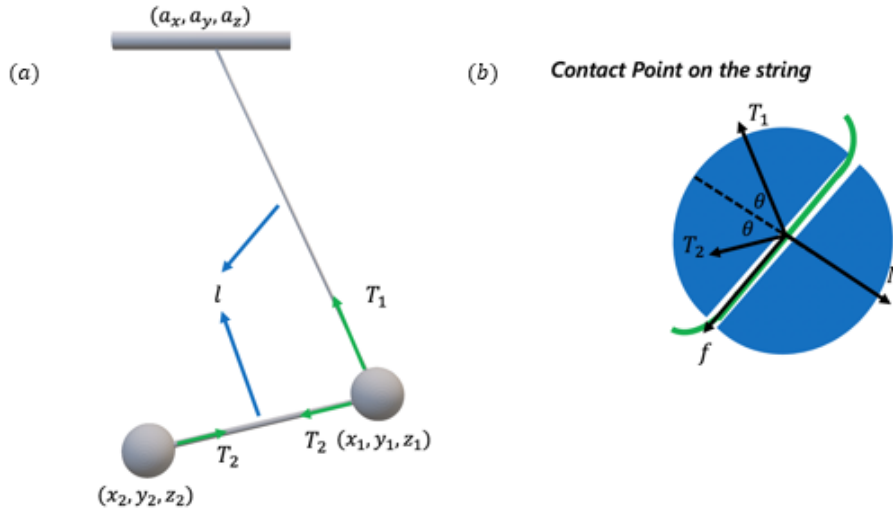
Figure 2: **Illustration of the geometry and coordinates in the Astrojax Pendulum.** (a) Coordinates of the point of suspension, middle ball and the bottom ball. T_1 and T_2 represents the tension exerted by the upper and bottom part of the string. (b) Force diagram of contact point on the string. Normal force N acts along the angle bisector of T_1 and T_2. θ is half the angle between the upper and bottom half of the string.

2.2 Lagrangian Formulation

We shall now derive the dynamical model of the Astrojax pendulum via Lagrangian mechanics. With the net kinetic and potential energy of the two balls, the Lagrangian of the system is as follows:

$$\mathcal{L} = \frac{1}{2}m\dot{q}^2 - mg(z_1 + z_2) \tag{1}$$

The inextensibility constraints are defined as

$$\alpha = \frac{1}{\sqrt{(x_1 - a_x)^2 + (y_1 - a_y)^2 + (z_1 - a_z)^2}} \tag{2}$$

$$\beta = \frac{1}{\sqrt{(x_2 - x_1)^2 + (y_2 - y_1)^2 + (z_2 - z_1)^2}} \tag{3}$$

$$\lambda(q) = \frac{1}{\alpha} + \frac{1}{\beta} - l = 0 \tag{4}$$

The Lagrange multiplier was included, which can be interpreted as the tension to maintain the constraints.

$$\mathcal{L} = \frac{1}{2}m\dot{q}^2 - mg(z_1 + z_2) - \boldsymbol{D}\lambda(q)\mu \tag{5}$$

Considering the friction between the string and the middle ball, two Lagrange multipliers μ_1, μ_2 are required for the two different tensions acting along the top-half and the bottom-half of the string.

$$\boldsymbol{D}\lambda(q)\mu = \begin{bmatrix} \alpha(x_1 - a_x)\mu_1 - \beta(x_2 - x_1)\mu_2 \\ \alpha(y_1 - a_y)\mu_1 - \beta(y_2 - y_1)\mu_2 \\ \alpha(z_1 - a_z)\mu_1 - \beta(z_2 - z_1)\mu_2 \\ \beta(x_2 - x_1)\mu_2 \\ \beta(y_2 - y_1)\mu_2 \\ \beta(z_2 - z_1)\mu_2 \end{bmatrix} \tag{6}$$

To account for non-conservative forces such as air drag, we employ the Rayleigh Dissipation function. For our case, the function is given by

$$W_{air} = \frac{1}{2}c_D\dot{q}^2 \tag{7}$$

Hence, the modified Euler-Lagrange equation is

$$\frac{d}{dt}\frac{\partial L}{\partial \dot{q}_i} - \frac{\partial L}{\partial q_i} = -\frac{\partial W_{air}}{\partial \dot{q}_i} \tag{8}$$

Now, we look at the force diagram of the contact point on the string as shown in Fig. 2(b). The two normal forces acting along the angle bisector are denoted as T_1 and T_2. Assuming the mass of string to be negligible, the forces present are always in equilibrium. Hence, the force balance equations are obtained as follow, where N is the normal force and f is the friction of the ball along the string.

$$\gamma = (x_1 - a_x)(x_2 - x_1) + (y_1 - a_y)(y_2 - y_1) + (z_1 - a_z)(z_2 - z_1) \tag{9}$$

$$N = (T_1 + T_2)cos\frac{cos^{-1}\alpha\beta\gamma}{2} \tag{10}$$

$$f = (T_1 - T_2)sin\frac{cos^{-1}\alpha\beta\gamma}{2} \tag{11}$$

Therefore, with Equations (4), (8), (9), (10) and (11), we can solve the motions of the balls numerically.

2.3   Numerical Solving Method

The high computational cost of the equations renders the use of *NDSolve* function in *MATHE-MATICA* futile [10]. Therefore, to numerically solve the equations, we manually discretise the equations by defining a time step k, arriving at the expressions of displacement, velocity and acceleration of the system at time step k as follows:

$$q^{(k)} = (x_1^{(k)}, y_1^{(k)}, z_1^{(k)}, x_2^{(k)}, y_2^{(k)}, z_2^{(k)}) \tag{12}$$

$$\dot{q}^{(k)} = \frac{q^{(k)} - q^{(k-1)}}{t} \tag{13}$$

$$\ddot{q}^{(k)} = \frac{\dot{q}^{(k)} - \dot{q}^{(k-1)}}{t} \tag{14}$$

where k is the time interval between two individual time steps, and this value is set as 1/2000 seconds in the simulation. With the expressions of displacement, velocity, and acceleration, we discretise the Euler-Langrange equation as follows:

$$m\frac{(q^{(k+1)} - 2q^{(k)} + q^{(k-1)})}{t^2} + \frac{\partial V}{\partial q} - \boldsymbol{D}\lambda(q^{(k)})\mu^{(k)} - c_D\frac{q^{(k)} - q^{(k-1)}}{t} = 0 \tag{15}$$

$$\frac{\partial V}{\partial q} = \begin{bmatrix} 0 \\ 0 \\ mg \\ 0 \\ 0 \\ mg \end{bmatrix} \tag{16}$$

$$\alpha^{(k)} = \frac{1}{\sqrt{(x_1^{(k)} - a_x^{(k)})^2 + (y_1^{(k)} - a_y^{(k)})^2 + (z_1^{(k)} - a_z^{(k)})^2}} \tag{17}$$

$$\beta^{(k)} = \frac{1}{\sqrt{(x_2^{(k)} - x_1^{(k)})^2 + (y_2^{(k)} - y_1^{(k)})^2 + (z_2^{(k)} - z_1^{(k)})^2}} \tag{18}$$

$$\boldsymbol{D}\lambda(q^{(k)})\mu^{(k)} = \begin{bmatrix} \alpha^{(k)}(x_1^{(k)} - a_x^{(k)})\mu_1^{(k)} - \beta^{(k)}(x_2^{(k)} - x_1^{(k)})\mu_2^{(k)} \\ \alpha^{(k)}(y_1^{(k)} - a_y^{(k)})\mu_1^{(k)} - \beta^{(k)}(y_2^{(k)} - y_1^{(k)})\mu_2^{(k)} \\ \alpha^{(k)}(z_1^{(k)} - a_z^{(k)})\mu_1^{(k)} - \beta^{(k)}(z_2^{(k)} - z_1^{(k)})\mu_2^{(k)} \\ \beta^{(k)}(x_2^{(k)} - x_1^{(k)})\mu_2^{(k)} \\ \beta^{(k)}(y_2^{(k)} - y_1^{(k)})\mu_2^{(k)} \\ \beta^{(k)}(z_2^{(k)} - z_1^{(k)})\mu_2^{(k)} \end{bmatrix} \tag{19}$$

The force balance equations at time step k can also be obtained as follow:

$$\gamma^{(k)} = (x_1^{(k)} - a_x^{(k)})(x_2^{(k)} - x_1^{(k)}) + (y_1^{(k)} - a_y^{(k)})(y_2^{(k)} - y_1^{(k)}) + (z_1^{(k)} - a_z^{(k)})(z_2^{(k)} - z_1^{(k)}) \tag{20}$$

$$N^{(k)} = (T_1^{(k)} + T_2^{(k)})cos\frac{cos^{-1}\alpha^{(k)}\beta^{(k)}\gamma^{(k)}}{2} \tag{21}$$

$$f^{(k)} = (T_1^{(k)} - T_2^{(k)})sin\frac{cos^{-1}\alpha^{(k)}\beta^{(k)}\gamma^{(k)}}{2} \tag{22}$$

Combining equations (15)-(22), we expand the generalised coordinate q into $(x_1, y_1, z_1, x_2, y_2, z_2)$ and arrive at the full equations of motion (23)-(28) and constraints (29)-(31) in discretised form.

$$m\frac{(x_1^{(k+1)} - 2x_1^{(k)} + x_1^{(k-1)})}{t^2} - \mu_1^{(k)}\alpha^{(k)}(x_1^{(k)} - a_x^{(k)}) + \mu_2^{(k)}\beta^{(k)}(x_2^k - x_1^{(k)}) - c_D\frac{x_1^{(k)} - x_1^{(k-1)}}{t} = 0 \tag{23}$$

$$m\frac{(y_1^{(k+1)} - 2y_1^{(k)} + x_1^{(k-1)})}{t^2} - \mu_1^{(k)}\alpha^{(k)}(y_1^{(k)} - a_y^{(k)}) + \mu_2^{(k)}\beta^{(k)}(y_2^k - y_1^{(k)}) - c_D\frac{y_1^{(k)} - y_1^{(k-1)}}{t} = 0 \tag{24}$$

$$m\frac{(z_1^{(k+1)} - 2z_1^{(k)} + z_1^{(k-1)})}{t^2} - \mu_1^{(k)}\alpha^{(k)}(z_1^{(k)} - a_z^{(k)}) + \mu_2^{(k)}\beta^{(k)}(z_2^k - z_1^{(k)}) + mg - c_D\frac{z_1^{(k)} - z_1^{(k-1)}}{t} = 0 \tag{25}$$

$$m\frac{(x_2^{(k+1)} - 2x_2^{(k)} + x_2^{(k-1)})}{t^2} - \mu_2^{(k)}\beta^{(k)}(x_2^{(k)} - x_1^{(k)}) - c_D\frac{x_2^{(k)} - x_2^{(k-1)}}{t} = 0 \tag{26}$$

$$m\frac{(y_2^{(k+1)} - 2y_2^{(k)} + y_2^{(k-1)})}{t^2} - \mu_2^{(k)}\beta^{(k)}(y_2^{(k)} - y_1^{(k)}) - c_D\frac{y_2^{(k)} - y_2^{(k-1)}}{t} = 0 \qquad (27)$$

$$m\frac{(z_2^{(k+1)} - 2z_2^{(k)} + z_2^{(k-1)})}{t^2} - \mu_2^{(k)}\beta^{(k)}(z_2^{(k)} - z_1^{(k)}) + mg - c_D\frac{z_2^{(k)} - z_2^{(k-1)}}{t} = 0 \qquad (28)$$

$$\frac{1}{\alpha^{(k+1)}} + \frac{1}{\beta^{(k+1)}} - l = 0 \qquad (29)$$

$$N^{(k)} = (\mu_1^{(k)} + \mu_2^{(k)})cos\frac{cos^{-1}\alpha^{(k)}\beta^{(k)}\gamma^{(k)}}{2} \qquad (30)$$

$$f^{(k)} = (\mu_1^{(k)} - \mu_2^{(k)})sin\frac{cos^{-1}\alpha^{(k)}\beta^{(k)}\gamma^{(k)}}{2} \qquad (31)$$

2.4 Constant Characterisation

In order to solve the discretised equations of motion derived in Section 2.3, we experimentally measured the constants involved, specifically the drag coefficient and both the static and the kinetic friction coefficients.

As shown in Fig. 3(a) and (b), we conducted a simple pendulum experiment and fitted a decay envelope to the pendulum's displacement-time graph to obtain the value of the drag coefficient $c_D = 1.7245 \times 10^{-3} kg/s$. Additionally, we also conducted a simple experiment with a ball and a tilted string to measure both the static and kinetic friction coefficients as shown in Fig. 3(c) and (d). The values of static and kinetic friction coefficients obtained are $\mu_{static} = 0.25676$ and $\mu_{kinetic} = 0.17176$.
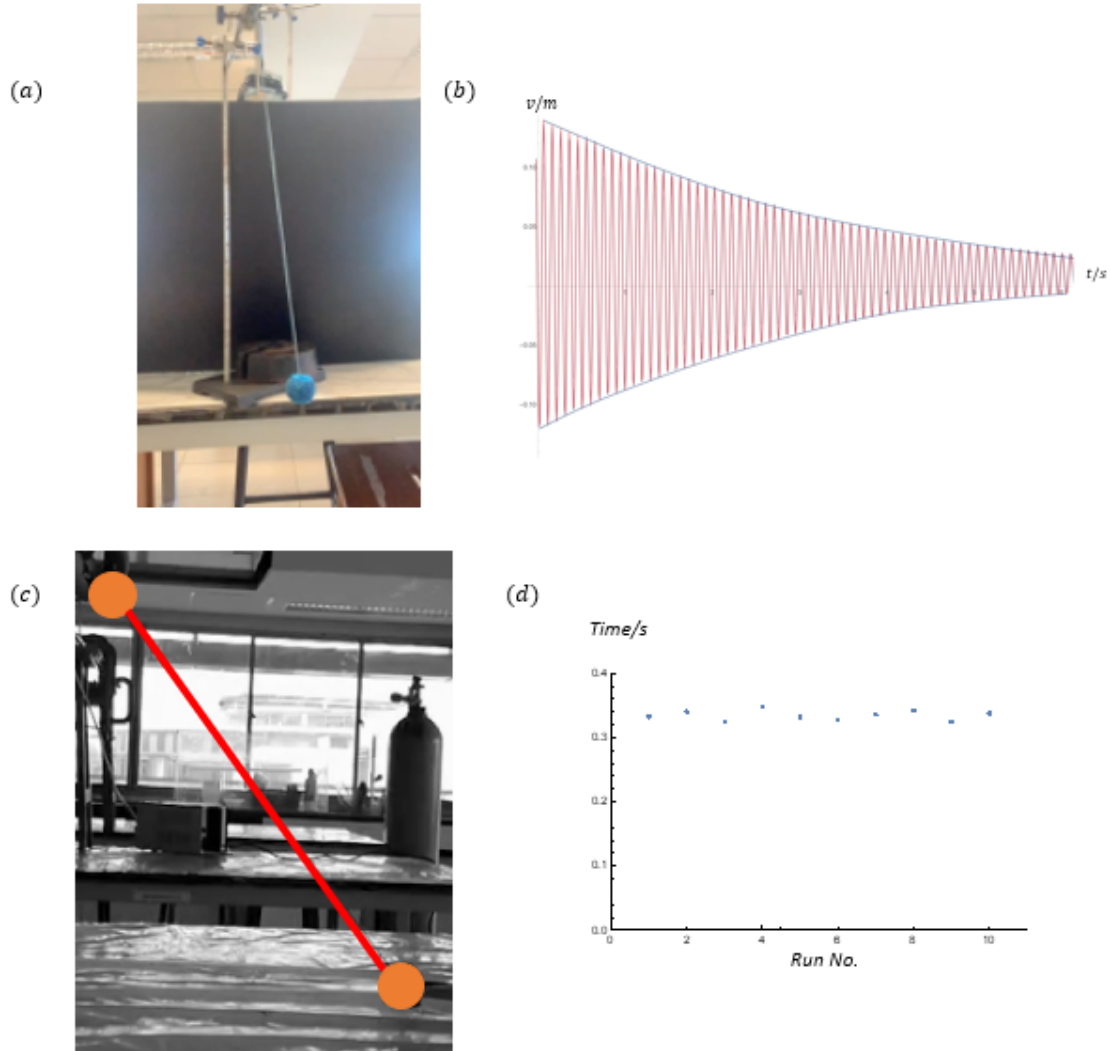
Figure 3: **Experimental setup for constant charactersiation.** (a) Experimental setup to measure drag coefficient. A single ball is set up as a simple pendulum and set into oscillation with small displacement. (b) Displacement-time graph of the pendulum. Fitting the decay envelope to the displacement-time graph of the pendulum, we could obtain the drag coefficient. (c) Setup to measure static and kinetic friction coefficients. Adjust the tilted angle of the string and measure the angle which the ball just starts to slide downwards to obtain the static friction coefficient. Track the displacement of the movement of the ball and measure its velocity for calculation of friction force based on force equilibrium. (d) Velocity of ball across multiple experiments.

3 Experimental Verification and Discussion

3.1 Experimental Setup

The experimental setup used is shown in Fig. 4. The length of the string used is 0.826 m, and the mass of balls is 0.018 kg. In Fig. 4(a), a rotating motor is used to drive the top end of the string. A mirror is placed below the pendulum at 45 degrees to allow for simultaneous tracking of both the bottom view and front view of the system. The coordinates of the balls are tracked at 240 fps with the open-source tracking software TRACKER [11]. Light is shined onto the white cardboard placed behind the pendulum to set up a strong contrast between the balls and the background to ease the automatic tracking process.

The distance between the camera and the equilibrium position of the pendulum was kept at approximately 2m to minimise parallax error. To obtain the 3D positions of the balls, we use the following method. The origin of the system is defined as the centre of the motor in both the front view picture and the bottom view captured from the mirror. The axes in the plane of the camera view were calibrated against a preset ruler. The (x, y) coordinates of the two balls from the front view in the camera's plane correspond to the (x_1, z_1) of the middle ball and (x_2, z_2) of the bottom ball, respectively. Meanwhile, the (x, y) coordinates of the balls from the bottom view in the camera's plane correspond to the (x_1, y_1) of the middle ball and (x_2, y_2) of the bottom ball, respectively.
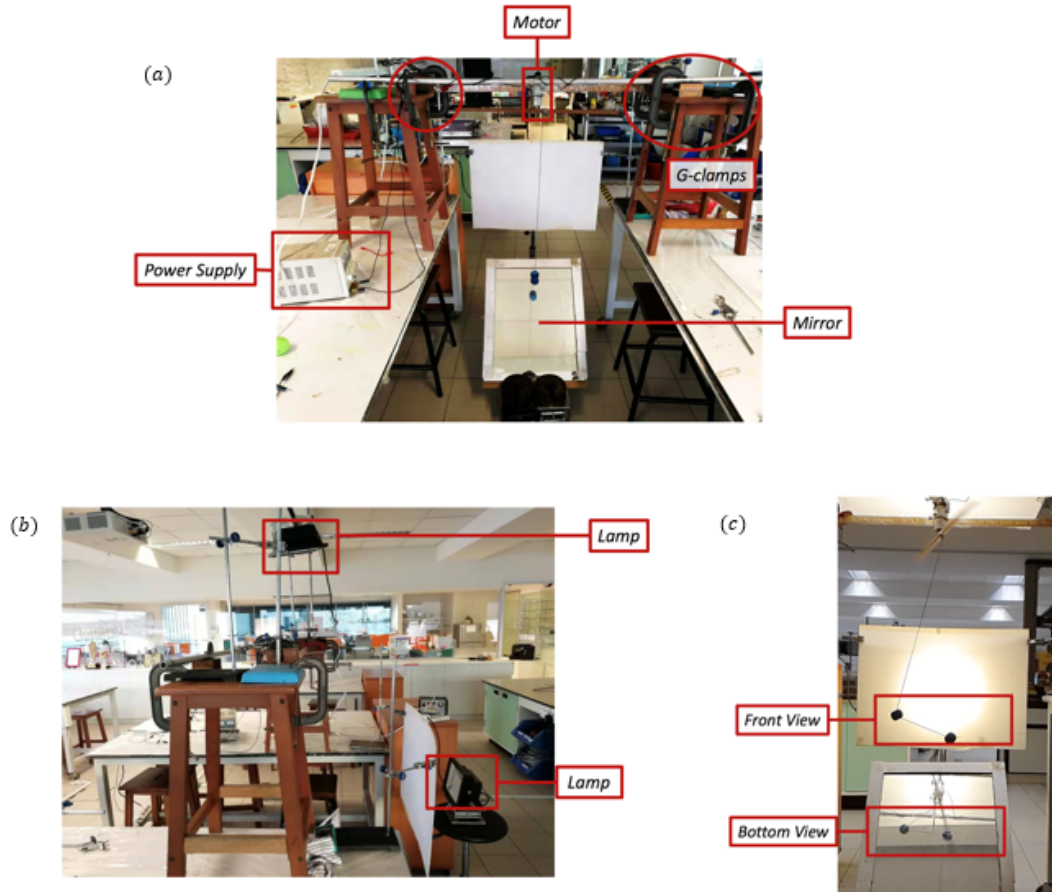
Figure 4: **Illustration of the geometry and coordinates in the Astrojax Pendulum.** (a) The front view of the experimental setup. A motor is connected to the top of the string via a horizontal rod. A power supply is connected to the motor to adjust its angular frequency. Multiple G clamps are used to prevent the set-up from shaking. A mirror set up at 45 degrees is used to obtain the bottom view of the motion of the two balls. (b) The side view of the experimental setup. Two lamps are positioned on the top of the motor and behind the balls respectively. This sets a strong contrast between the balls and the background to ease tracking. (c) Front and bottom views of balls for tracking.

3.2 Dynamic Trajectories

3.2.1 Hysteresis in Rising and Falling Motions

To start the motion of the pendulum, the pendulum was first suspended vertically with the two balls held at the bottom of the string. The angular frequency of the motor was gradually increased. Upon the threshold frequency of $\omega_{rise} = 12.63\pi rad/s$, which was experimentally determined, the middle ball would start to move up along the string. With any angular frequency lower than the value of ω_{rise}, the two balls would remain at the bottom as seen in the supplementary video (see Video S1 and S2).

The angular frequency of motor was then gradually decreased. The orbits of the balls remained circular until motor frequency decreased lower than $\omega_{fall} = 3.24\pi rad/s$, where the middle ball moved down the string. Videos in the supplementary material of motor's angular frequency at $3.81\pi rad/s$ and $3.24\pi rad/s$ demonstrate this critical value of $\omega_{fall} = 3.24\pi rad/s$ for falling (see Video S3 and S4 respectively). Quantitatively, the theoretical motion path of the balls were plotted in Fig. 5(a) and (b). When the motor frequency ω_m drops to $3.24\pi rad/s$, the balls would drop from their stable orbits in Fig. 5(a) to the orbits in Fig. 5(b).

This hysteresis region between ω_{fall} and ω_{rise} could be explained qualitatively using force analysis of the middle ball in a rotation frame. In Fig. 5(c), when the relation $F_c cos\theta > f + W sin\theta$ is satisfied, the force acting on the middle ball is not enough to counter the centrifugal force. Therefore, the resolved net force points upwards along the string, causing the middle ball to move up. Similarly, the middle ball moves down when the relation $F_c cos\theta < W sin\theta + f$ is satisfied. The direction of friction f is therefore the key reason for the difference in ω_{rise} and ω_{fall}.

14
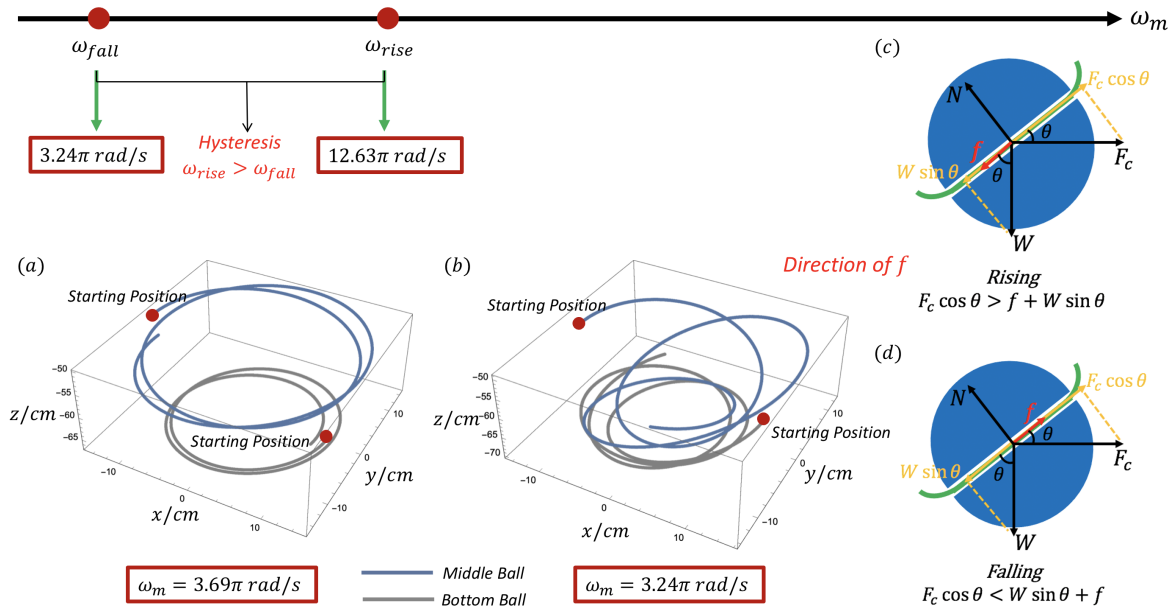
Figure 5: **Illustration of hysteresis in rising and falling motions.** (a) Stable orbits of middle and bottom balls with motor frequency $\omega_m = 3.69\pi rad/s$. (b) When motor frequency ω_m reaches $\omega_{fall} = 3.24 rad/s$, the balls drop from their stable orbits. (c) Labeled force diagram of rising mechanism. F_c denotes the centrifugal force experienced by the middle ball in the rotation frame. W represents the weight of the middle ball. (d) Labeled force diagram of falling mechanism.
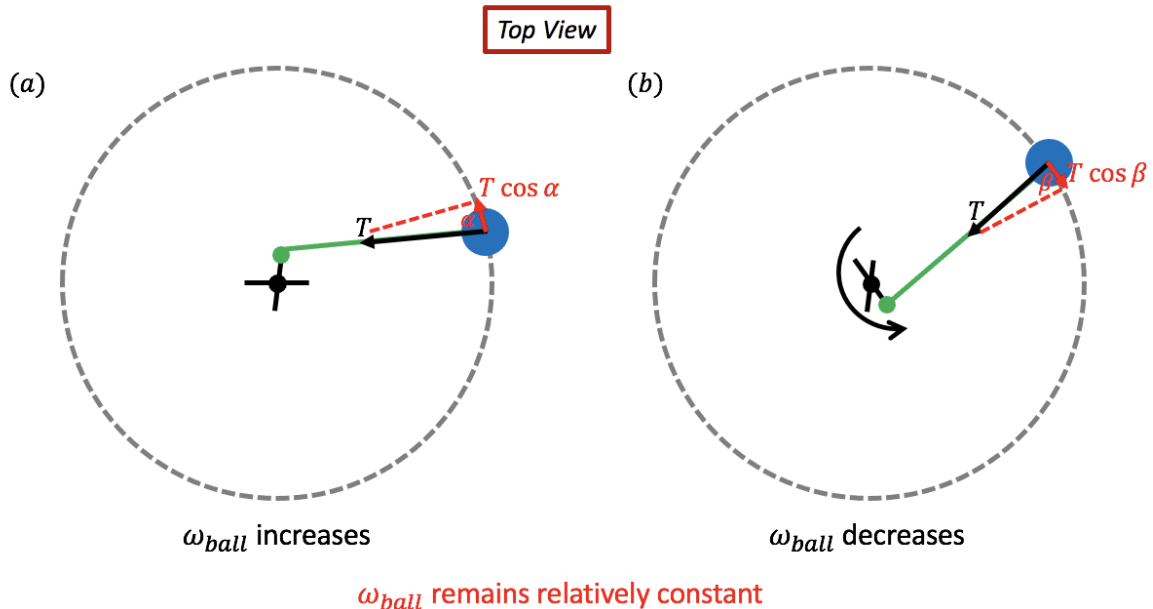
Figure 6: **Top view of the experimental setup when** $\omega_m > \omega_{ball}$ (a) Force analysis when ω_m is slightly greater than ω_{ball}. (b) Force analysis when ω_m is much greater than ω_{ball}.

3.2.2 Circular Orbits

Before reaching the value of $\omega_{fall} = 3.24\pi rad/s$, the motor frequency could be increased gradually to attain a stable circular orbit with $\omega_m = \omega_{ball}$. A demonstration video of circular orbit could be found in the supplementary material (see Video S5 and S6). An angular frequency ω_1 of $4.80\pi rad/s$ is experimentally determined to be the maximum value required to maintain the same speed for both the motor and the balls. If ω_m is greater than ω_1, the motor will spin faster than the ball, as shown by the experimental videos of $\omega_m = 5.00\pi rad/s$ and $\omega_m = 4.80\pi rad/s$ in the supplementary material (see Video S7 and S8 respectively).

To qualitatively explain this, we look at the motion from top view shown in Fig. 6. When we increase ω_m, the motor experiences a greater angular displacement, and we obtain the position of the middle ball in Fig. 6(a). Tension exerted on the middle ball has a tangential component $T cos\alpha$ to increase ω_{ball}, so that the ball can catch up with the motor. However, if ω_m is too high, before the ball can catch up with the motor, we observe the position of ball in Fig. 6(b). The tangential component of tension $T cos\beta$ will decrease ω_{ball}. Therefore, for one cycle, the angular velocity of the balls increases and decreases periodically, making ω_{ball} relatively constant throughout the motion.

Different combinations of ω_m and ω_{ball} can be obtained by further increasing the motor frequency ω_m until the value of $\omega_2 = 15.00\pi rad/s$, where ω_2 was experimentally determined to be the maximum motor frequency to maintain a stable circular orbit. Videos of $\omega_m = 16.00\pi rad/s$ and $\omega_m = 15.00\pi rad/s$ are provided in the supplementary material to demonstrate the phenomenon that when the motor frequency exceeds the threshold value, no more circular orbits would be observed (see Video S9 and S10). Motion paths of both the middle and the bottom balls were plotted at various values of ω_m, as shown in Fig. 7 (a)-(h), where a good agreement between theory and experiments was obtained.

We will now look at the relation between ω_m and ω_{ball} in Fig. 7(i). From the simulation for the motion path, we calculated the period of the motion and therefore the angular velocity of the balls. Plotting ω_{ball} against ω_m when there is a stable circular orbit, we obtained the three critical values – ω_{fall}, ω_1, and ω_2. Between ω_{fall} and ω_1, we notice that the speed of the balls increases with that of that motor. From ω_1 to ω_2, the speed of the balls remains constant when the speed of the motor keeps increasing.
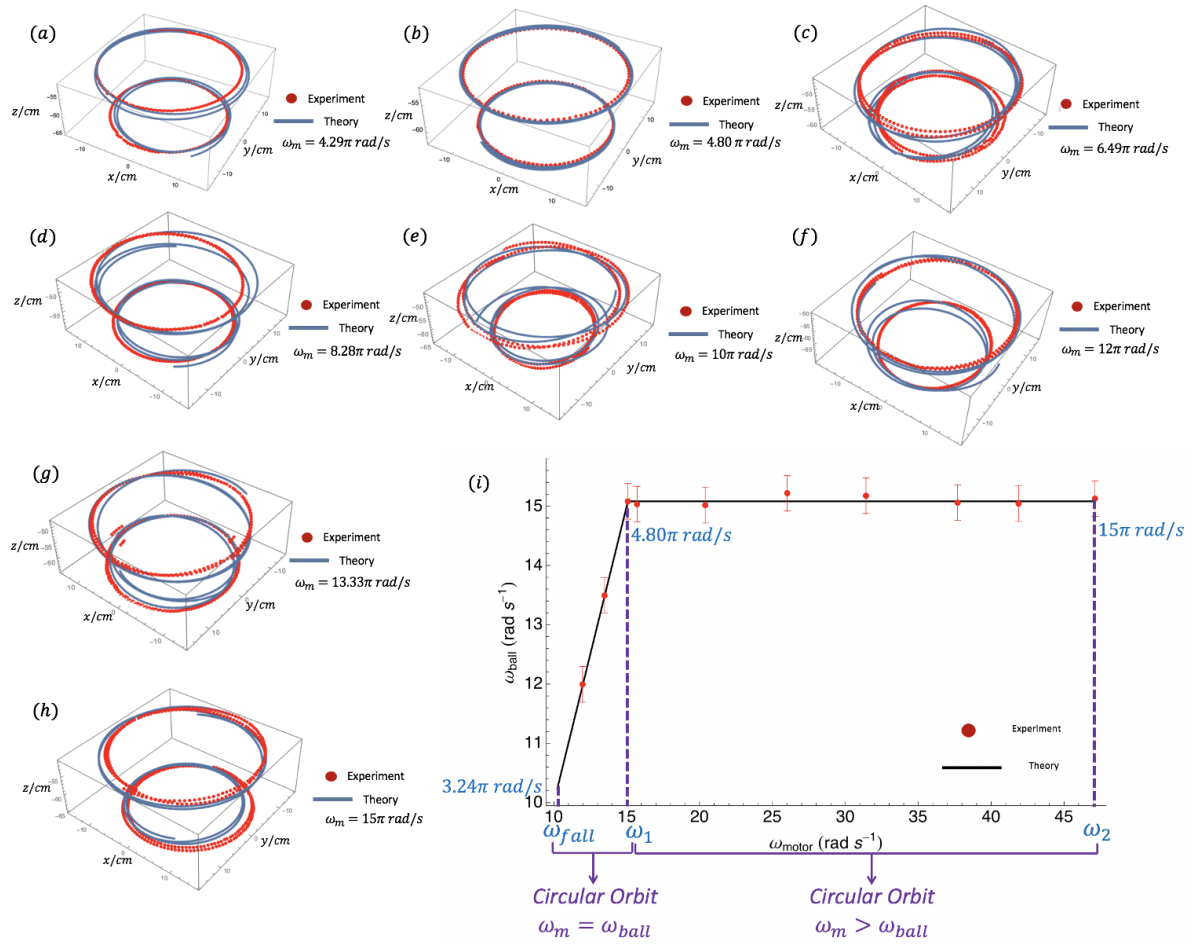
Figure 7: **Theoretical and experimental motion paths of circular orbits.** (a)-(h) Circular motion paths of both the middle and the bottom balls at various ω_m values. (i) Plot of ω_{ball} against ω_m.

3.2.3 Flower Orbits

When ω_m is increased beyond the value of ω_2, a flower orbit of the balls can be observed. A demonstration video of the flower motion is provided in the supplementary material (see Video S11 and S12). In Fig. 8(a), the two balls undergo circular motion about their own symmetry axes, while the entire system spins about the symmetry axis of the motor. A demonstration video visualised in *MATHEMATICA* could also be found in the supplementary material (see Video S13). The top projection of both the experimental and theoretical trajectories of both the middle and the bottom balls are plotted in Fig. 8(b)-(c) and (d)-(e), respectively. While a qualitative trend could be well predicted by our theoretical model, the lack of accurate alignment between experimental and theoretical plots is due to the failure of length constraint of the string – the large angular velocity of motor provides enough centripetal force for the string, making it a convex shape as shown in Fig. 8(f).
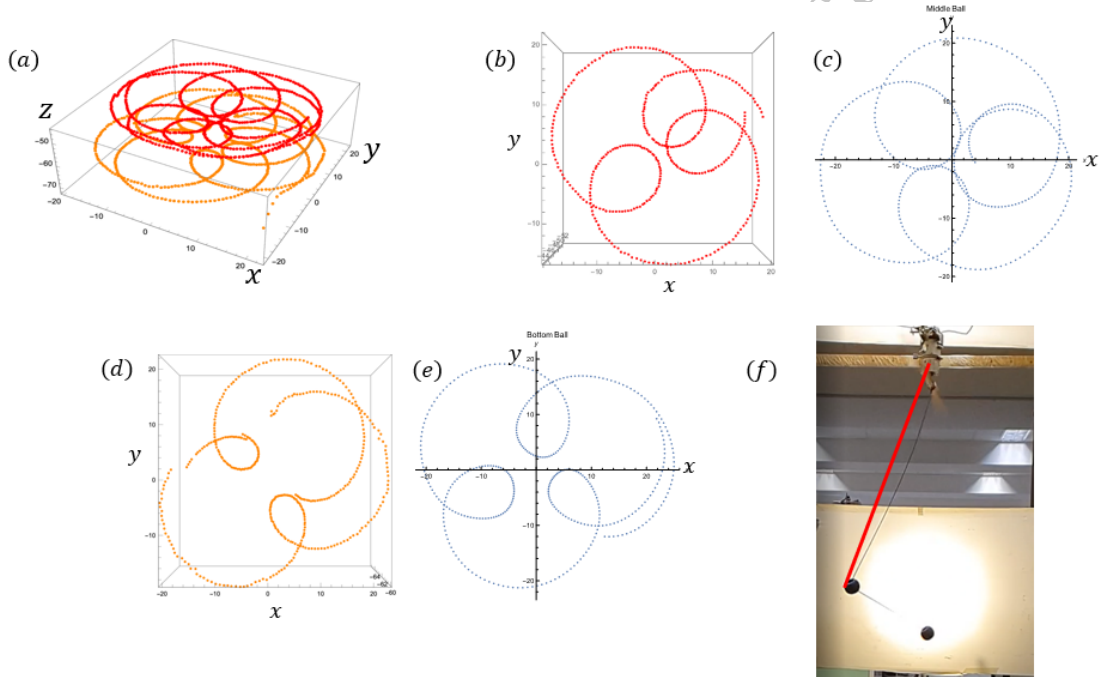
Figure 8: **Theoretical and experimental motion paths of flower orbits.** (a) Experimental trajectories of middle and bottom balls. (b)-(c) Top projection of (b)experimental and (c)theoretical trajectories of middle ball. (d)-(e) Top projection of (d)experimental and (e)theoretical trajectories of bottom ball. (f) Experiment illustration on slack string during flower motion.

3.3 Effect of Varying Parameters on Circular Orbits

Thus far, we have completed a comprehensive discussion on how the motion paths of balls evolve upon different angular velocities of motor. Taking the stable circular orbit, we therefore go a step further to discuss the effect of various parameters on the system.

In Fig. 9(a) and (b), both the experimental and theoretical motion paths of the two balls are obtained with $\omega_m = \omega_{ball} = 4.8\pi rad/s$, $m_1 = m_2 = 0.018kg$ in (a) and $m_1 = m_2 = 0.1kg$ in (b). We observe that when mass of the balls increases, there is no significant change in the orbits while tension along the string increases proportionally. Similarly, in Fig. 9(c) and (d), experimental and theoretical motion paths are obtained with $\omega_m = 15\pi rad/s$, $= \omega_{ball} = 4.80\pi rad/s$, and $m_1 = m_2 = 0.018kg$ in (c) and $m_1 = m_2 = 0.1kg$ in (d). No significant change in the motion paths of balls are resulted.

With the conditions of $\omega_m = \omega_{ball} = 4.8\pi rad/s$, $l = 0.826m$ in (e) and $l = 0.662m$ in (f), we obtained similar circular orbits as well. Increasing the motor angular frequency to $\omega_m = 15.0\pi rad/s$, circular orbits remain approximately the same as shown in Fig. 9(g) and (h).

Our experimental results show that varying the mass of the balls and the total length of the string within a relatively small range does not alter the qualitative patterns of the stable circular motion significantly. However, this does not necessarily imply that these circular orbits are quantitatively the same. Instead, considering that such a circular motion system could be solved exploiting the Newton's Second Law, where we equate the net force to the centripetal force provided by the motor on the balls, we unexpectedly notice that with the same parameters (i.e. the same mass of balls, string length, radius of circular orbits, and angular velocity of motor), there would be multiple solutions obtained, which correspond to multiple stable circular orbits at a given centripetal force. Additionally, the value of centripetal force is determined by a total of three parameters – the x-coordinate of the point of suspension a_x, angular velocity of the motor ω_m, and the total length of the string l. Therefore, theoretically, it is possible for us to obtain various sets of centripetal force that each has its own subset of circular orbits as well. However, as we are unable to initiate the motion of the balls directly from a circular orbit (i.e. we were only able to start motion of balls from their stationary positions at the bottom.), we were not able to conduct a complete investigation on all possible subsets of circular orbits in the system. Nonetheless, this could certainly be an interesting investigation to undertake for future studies.

19

(a) $\omega_m = \omega_{ball} = 4.8\pi\ rad/s$
$m_1 = m_2 = 0.018kg$

(b) $\omega_m = \omega_{ball} = 4.8\pi\ rad/s$
$m_1 = m_2 = 0.1kg$

(c) $\omega_m = 15.0\pi\ rad/s$
$\omega_{ball} = 4.80\pi\ rad/s$
$m_1 = m_2 = 0.018kg$

(d) $\omega_m = 15.0\pi\ rad/s$
$\omega_{ball} = 4.80\pi\ rad/s$
$m_1 = m_2 = 0.1kg$

(e) $\omega_m = 4.8\pi\ rad/s$
$l = 0.826\ m$

(f) $\omega_m = 4.8\pi\ rad/s$
$l = 0.662\ m$

(g) $\omega_m = 15.0\pi\ rad/s$
$\omega_{ball} = 4.8\pi\ rad/s$
$l = 0.826\ m$

(h) $\omega_m = 15.0\pi\ rad/s$
$\omega_{ball} = 4.8\pi\ rad/s$
$l = 0.662\ m$
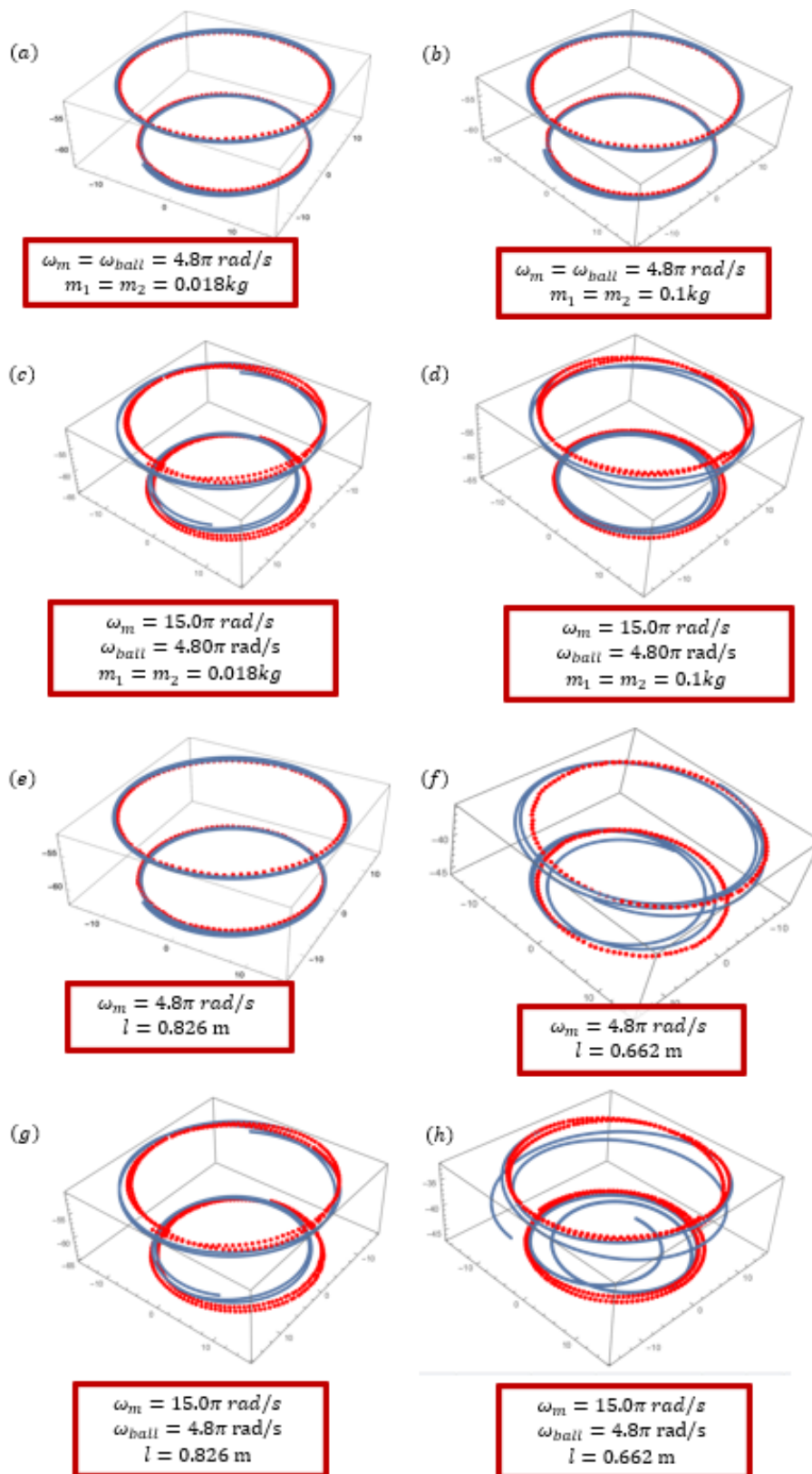
Figure 9: **Theoretical and experimental motion paths of circular orbits upon changing in parameters.**

3.4 Chaos

To determine whether chaos is present in the system, an infinitesimal change is implemented in the initial condition (Table. 1), and no significant deviation in both circular motion (Fig. 10(a) and (b)) and flower motion (Fig. 10(c) to (f)) is resulted.

Initial Conditions	Circular Orbit 1	Circular Orbit 2	Flower Orbit 1	Flower Orbit 2	Flower Orbit 3	Flower Orbit 4
$x_1^{(0)}$	-14.427	-14.426	3.937	3.837	3.937	3.837
$x_1^{(1)}$	$-14.427\mathrm{Cos}\theta$	$-14.427\mathrm{Cos}\theta$	3.568	3.568	3.568	3.468
$y_1^{(0)}$	0	0	-0.426	-0.416	-0.406	-0.426
$y_1^{(1)}$	$14.427\mathrm{Sin}\theta$	$14.428\mathrm{Sin}\theta$	-0.014	-0.014	-0.014	-0.014
$z_1^{(0)}$	-52.483	-52.484	-51.755	-51.775	-51.775	-51.775
$z_1^{(1)}$	-52.483	-52.483	-51.783	-51.783	-51.783	-51.783
$x_2^{(0)}$	11.924	11.924	21.817	21.817	22.817	22.817
$x_2^{(1)}$	11.924	11.924	22.251	22.251	22.251	22.251
$y_2^{(0)}$	0	0	9.257	9.257	9.257	9.257
$y_2^{(1)}$	-11.924	-11.924	8.569	8.569	8.569	8.569
$z_2^{(0)}$	-62.353	-62.353	-60.846	-60.846	-60.846	-60.846
$z_2^{(1)}$	-62.353	-62.353	-60.846	-60.846	-60.846	-60.846

Table 1: Initial conditions of both circular and flower orbits.
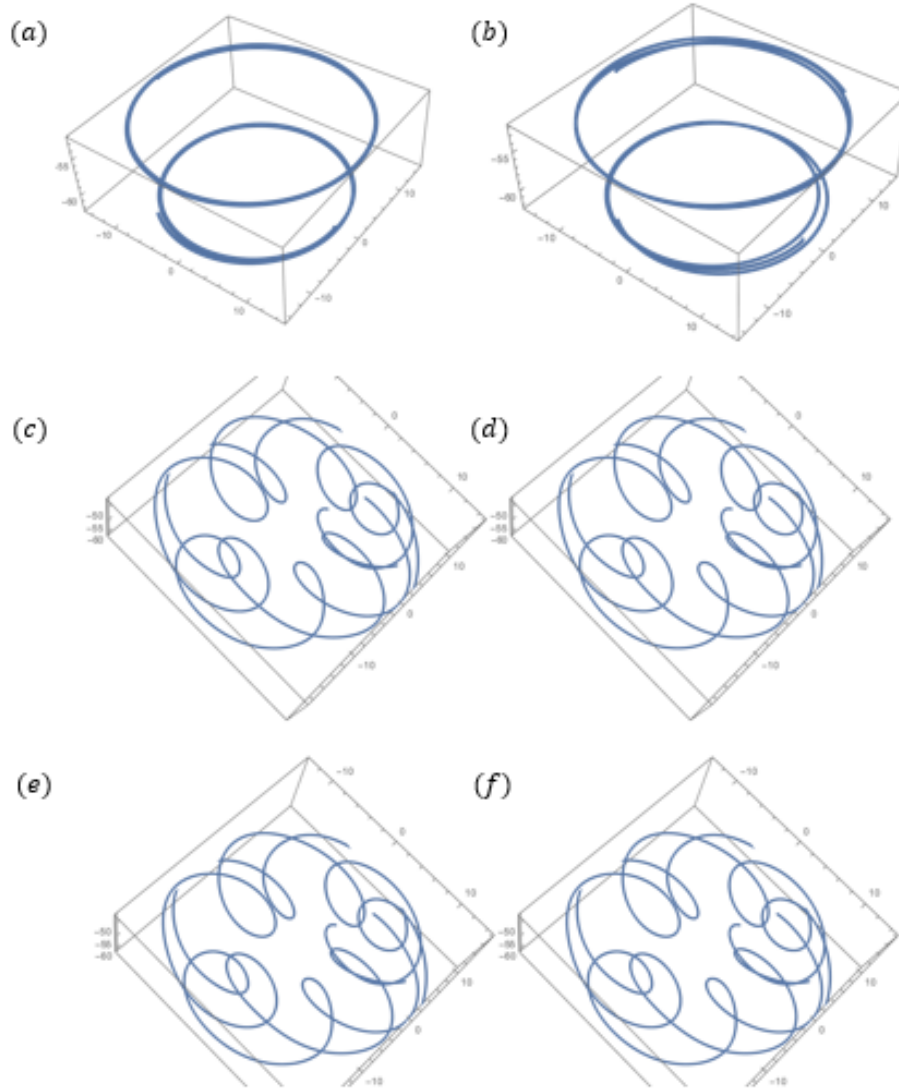
Figure 10: **Theoretical motion paths of circular orbits.** Initial conditions are shown in **Table 1**. (a)-(b) Circular orbit 1-2; (c)-(f) Flower orbit 1-4.

4   Future Work

As shown in the demonstration video of the Astrojax pendulum (see Video S14 in supplementary material), the motion of the Astrojax pendulum evolves over time, necessitating the study of time-dependent system an interesting topic for future exploration.

We first define the precession angle ϕ of the system as the angle between the vertical axis and the line from the center of the two balls to the origin as shown in Fig. 11(a). The motion of the pendulum could be initiated with the two balls staying at the bottom of the string as shown in Fig. 11(b). As the motor continues to impart energy into the system, the middle ball starts to rise up along the string, and the precession angle ϕ increases as shown in Fig. 11(c). During this process, the two balls exhibit a flower orbit that evolves over time as the middle ball keeps rising and the distance between the two balls increases. Eventually, the middle ball reaches its maximum displacement along the string (Fig. 11(d)), and the flower orbit now stabilises into a circular orbit for a short period of time (i.e. 10 seconds). Afterwards, the middle ball starts to fall, and the two balls enter the flower orbit again with its precession angle ϕ increasing continuously (Fig. 11(e)). Towards the end, the middle ball will fall to the bottom. The flower orbit will transform into a circular orbit again, as the Astrojax pendulum will approach a single spherical pendulum system where the two balls will be swung by the motor together.

However, a time-dependent study of the phenomena described in the previous paragraph is currently not feasible within the scope of this work primarily due to two reasons. Firstly, it can be deduced from the previous analysis that the flower orbit is a transient phase between the initiation, the intermediate stable circular orbit, and the final single pendulum system. As the system evolves, the state of the middle ball changes, and the friction between the middle ball and the string transits between static friction and kinetic friction. Hence, in order to accurately model the movement of the middle ball and thereby predict the motion path of the pendulum system, an upgraded Lagrangian theory that incorporates the stick-slip transition model (Fig. 12) is required. However, such stick-slip model is difficult to be implemented in our contemporary *MATHEMATICA* code, as it requires checking of the transition condition in every single time step, which simply incurs too much computational burden. Secondly, one complete evolution cycle of the pendulum lasts more than 10 minutes, where our contemporary numerical solver could not function for such prolonged period of time with high accuracy and precision. Nonetheless, using more advanced programming languages, such as Julia that is specially designed for numerical analysis [12], could circumvent such a problem.
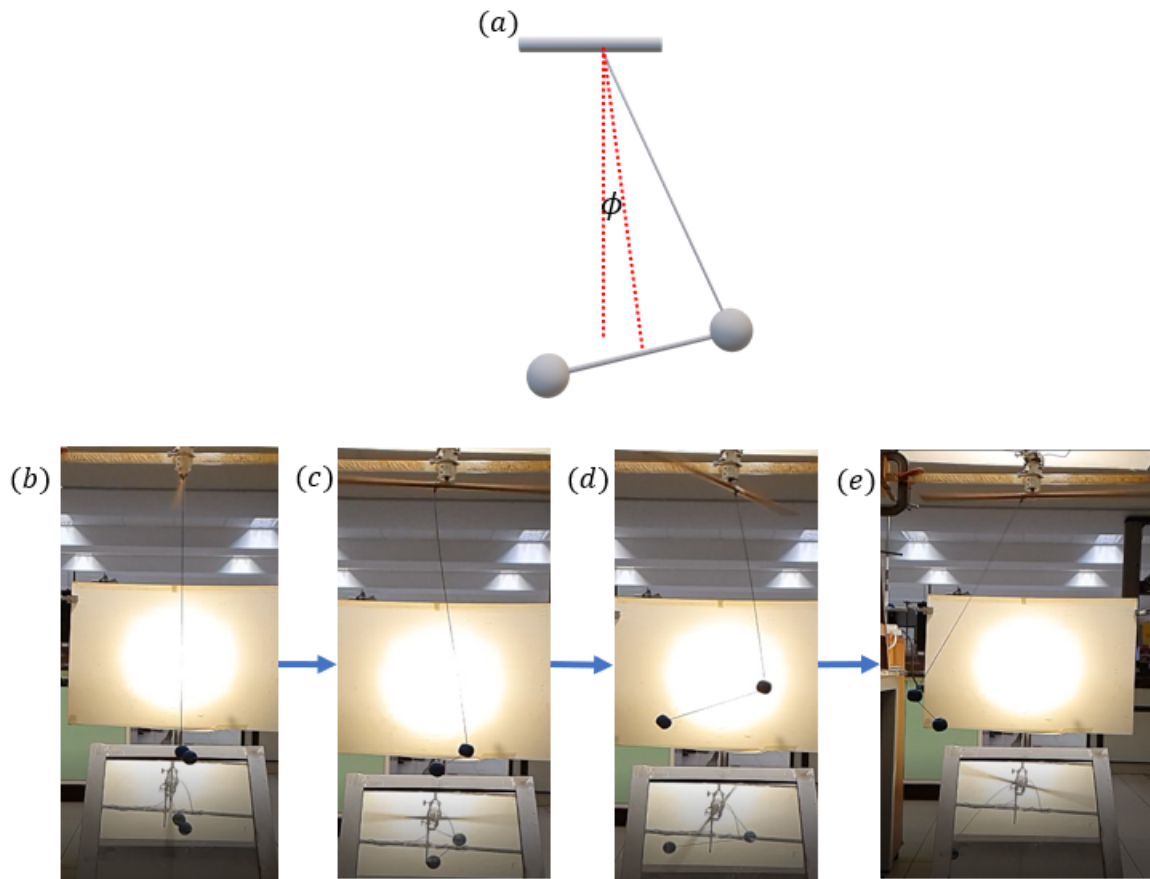
Figure 11: **Time evolution of motion of the Astrojax pendulum.** (a) Precession angle ϕ of the system. (b)-(e) Time dependent motion of the system.
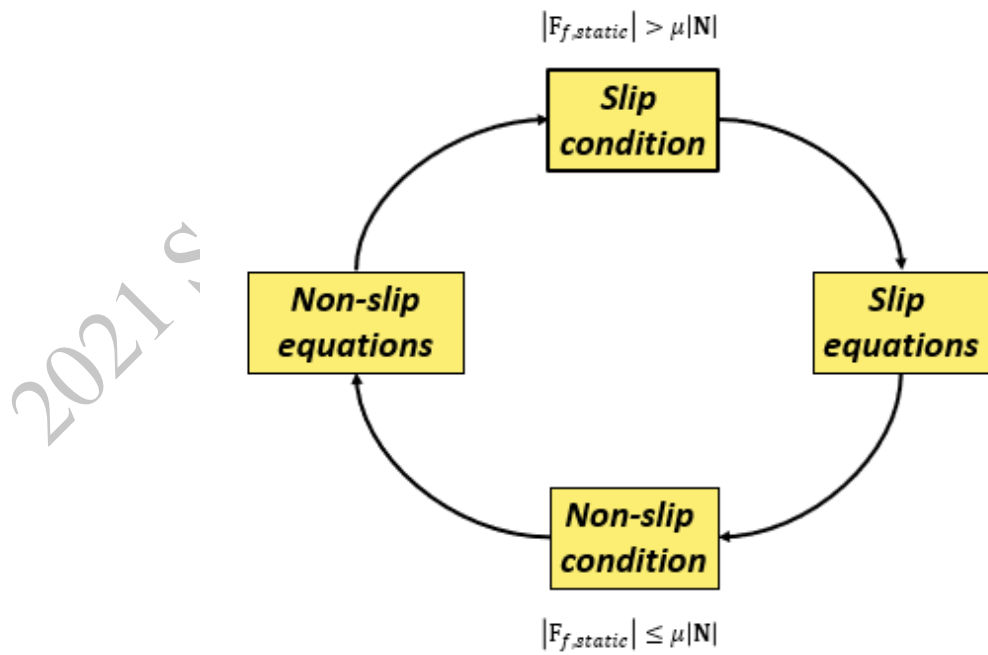
Figure 12: **Stick-slip transition model.**

5 Conclusion

In this work, we have explored the trajectories of both the middle and the bottom balls of an Astrojax pendulum under various angular frequencies of the top motor which was exploited to imitate the real-life condition of hand swinging. Qualitative explanations were provided on the hysterisis present in the rising and falling mechanisms of the middle ball based on a comprehensive force analysis. We discovered two regions for balls to exhibit circular motion – $\omega_m = \omega_{ball}$ (motor and balls have the same angular velocity) and $\omega_m > \omega_{ball}$ (balls are lagging behind the motor). We have also established a quantitative model based on Lagrangian mechanics and contact point analysis, solved it numerically using the method of discretisation, and provided satisfying comparison between theoretical and experimental trajectories of the two balls. The effect of varying parameters, such as total length of string and mass of the balls, were analysed as well. Additionally, the presence of chaos was also investigated by applying an infinitesimal change in the initial conditions and comparing the resultant motion trajectories.

The Astrojax pendulum is a simple system, yet it exhibits great educational merits in real-life application. For students who are interested in constructing a similar setup, a commercial Astrojax toy could be purchased easily, and an EV3 Lego motor could be used to provide the top spin. With regards to theory, the mathematics involved in this work, including Lagrangian mechanics and equilibrium force analysis, are well included in the syllabus of an undergraduate physics course, rendering it an excellent tool for class demonstration. The method of discretisation presented in this work also helps readers to improve the accuracy of their numerical solution, surmounting the large numerical error introduced using standard numerical methods such as *NDSolve* in *MATHEMATICA*. Moreover, the physics of the Astrojax pendulum can be extended to a theory called "reduction theory for mechanical system with symmetry", which is required in a variety of engineering applications, such as design of rotors of spacecrafts and underwater vehicle dynamics [13].

References

[1] Astrojax Toy: Educational Toy: Orbiting Toy. ASTROJAX. (n.d.). https://astrojax.com/.

[2] Campbell, C., Harrington, S., Karsai, A. (n.d.). Variable Length Spherical Pendulum: The Astrojax.

[3] Van Dooren, R. (1996). Chaos in a pendulum with forced horizontal support motion: a tutorial. Chaos, Solitons Fractals, 7(1), 77–90. https://doi.org/10.1016/0960-0779(95)00018-6

[4] Marsden, J. E., Scheurle, J. (1993). Lagrangian reduction and the double spherical pendulum. ZAMP Zeitschrift Für Angewandte Mathematik Und Physik, 44(1), 17–43. https://doi.org/10.1007/bf00914351

[5] Korsch, H. J., amp; Jodl, H.-J. (1999). The double pendulum. Chaos, 89–114. https://doi.org/10.1007/978-3-662-03866-6$_5$

[6] Marcelo Tusset, A., Piccirillo, V., Bueno, A. M., Manoel Balthazar, J., Sado, D., Felix, J. L., amp; Brasil, R. M. (2016). Chaos control and sensitivity analysis of a double Pendulum ARM excited by an RLC circuit BASED Nonlinear shaker. Journal of Vibration and Control, 22(17), 3621–3637. https://doi.org/10.1177/1077546314564782

[7] Karsai, A., Harrington, S., Campbell, C. (n.d.). The Astrojax Pendulum.

[8] Toit, P. D. (2005). The Astrojax Pendulum and the N-Body Problem on the Sphere: A Study in reduction, variational integration, and pattern evocation.

[9] Dichter, D., Maschan, K. (n.d.). Modeling and Simulation of Astrojax.

[10] Wolfram Mathematica. Wolfram Mathematica: Modern Technical Computing. (n.d.). https://www.wolfram.com/mathematica/.

[11] Tracker: Video Analysis and Modelling Tool. Tracker Video Analysis and Modeling Tool for Physics Education. (n.d.). https://physlets.org/tracker/.

[12] Jeff Bezanson, S. K. (n.d.). The julia programming language. The Julia Programming Language. https://julialang.org/.

[13] Marsden, J. E., amp; Ratiu, T. S. (2009). Mechanical systemsmechanical systems : Symmetries and reduction. Encyclopedia of Complexity and Systems Science, 5482–5510. https://doi.org/10.1007/978-0-387-30440-3$_3$26

A list of supplementary materials is provided in the next page.

Supplemental Information linked to this report include:

Video S1 Ball remains at bottom ($\omega_m = 12\pi rad/s$)

Video S2 middle ball rises ($\omega_m = 12.63\pi rad/s$)

Video S3 ($\omega_m = 3.81\pi rad/s$)

Video S4 ($\omega_m = 3.24\pi rad/s$)

Video S5 Circular Orbit front view

Video S6 Circular Orbit bottom view

Video S7 motor moves faster ($\omega_m = 5.00\pi rad/s$)

Video S8 ($\omega_m = \omega_{balls} = 4.80\pi rad/s$)

Video S9 ($\omega_m = 16.00\pi rad/s$)

Video S10 ($\omega_m = 15.00\pi rad/s$)

Video S11 Flower Motion front view

Video S12 Flower Motion bottom view

Video S13 Flower Motion Animation

Video S14 Overall Motion